POLITECNICO DI TORINO
Repository ISTITUZIONALE

Discrimination of glioma patient-derived cells from healthy astrocytes by exploiting Raman spectroscopy

(Article begins on next page)

01 September 2025

Discrimination of glioma patient-derived cells from healthy astrocytes by exploiting Raman spectroscopy

Nerea Iturrioz-Rodríguez [a,*], Daniele De Pasquale [a], Pietro Fiaschi [b,c], Gianni Ciofani [a,*]

[a] *Istituto Italiano di Tecnologia, Smart Bio-Interfaces, Viale Rinaldo Piaggio 34, 56025 Pontedera, Italy*
[b] *San Martino Policlinico Hospital, Department of Neurosurgery, IRCCS for Oncology and Neurosciences, Largo Rosanna Benzi 10, 16132 Genova, Italy*
[c] *University of Genoa, Department of Neurosciences, Rehabilitation, Ophthalmology, Genetics, Maternal and Child Health (DiNOGMI), Largo Paolo Daneo 3, 16132 Genova, Italy*

HIGHLIGHTS

- Raman spectroscopy, in particular in the range 1000–1300 cm^{-1}, was used to distinguish healthy astrocytes from glioma patient-derived cells.
- Peaks related to DNA/RNA and cytochrome c have been found increased in glioma cells.
- PCA-LDA analysis discriminated cancer cells from healthy astrocytes with an average accuracy of 92.5%.

GRAPHICAL ABSTRACT
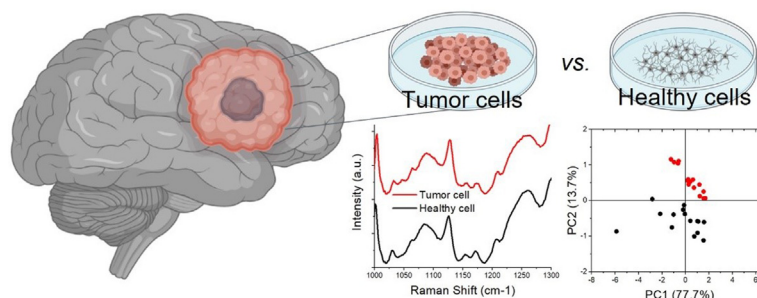
ARTICLE INFO

ABSTRACT

Glioblastoma multiforme (GBM) is one of the most common and aggressive brain tumors. It presents a very bad prognosis with a patients' overall survival of 12–15 months; treatment failure is mainly ascribable to tumor recurrence. The development of new tools, that could help the precise detection of the tumor border, is thus an urgent need. During the last decades, different vibrational spectroscopy techniques have been developed to distinguish cancer tissue from heathy tissue; in the present work, we compared GBM cells deriving from four patients with healthy human astrocytes using Raman spectroscopy. We have shown that the region between 1000 and 1300 cm^{-1} is enough informative for this discrimination, indeed highlighting that peaks related to DNA/RNA and cytochrome c are increased in cancer cells. Finally, our model has been able to discriminate cancer cells from healthy cells with an average accuracy of 92.5%. We believe that this study might help to further understand which are the essential Raman peaks exploitable in the detection of cancer cells, with important perspectives under a diagnostic point of view.

1. Introduction

Glioblastoma multiforme (GBM) is known for being the most common and aggressive brain cancer. It is composed by poorly differentiated astrocytic cancer cells that proliferate and invade normal brain parenchyma. It has a worldwide incidence rate of around 3 *per* 100.000 people with a 1.6 times higher incidence in men than women, and a higher frequency of primary GBMs in men and secondary GBMs in women [1–3]. Despite the current treatment that includes surgery followed by adjuvant radiotherapy and chemotherapy, the overall survival of the patients is just 12–15 months [2,4], in most of case because of tumor recurrence. Different studies have shown that the 80–90% of recurrences usually occur near the original resection margins, suggesting a partial fail-

* Corresponding authors.
E-mail addresses: nerea.iturrioz@iit.it (N. Iturrioz-Rodríguez), gianni.ciofani@iit.it (G. Ciofani).

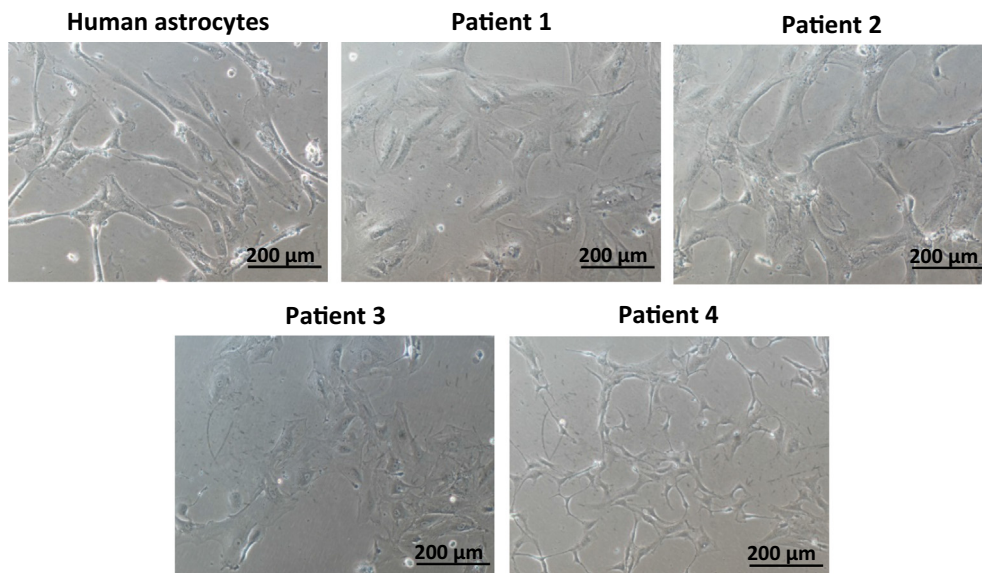**Human astrocytes** **Patient 1** **Patient 2**

Patient 3 **Patient 4**

Fig. 1. Representative bright field images of the cell cultures used in this work.

ure of resection surgery followed by radiotherapy and chemotherapy [5–8]. Hence, there is a strong need of developing new tools that detect the tumor border precisely, so that the tumoral mass can be resected completely, in order to improve the overall survival of patients.

Raman spectroscopy is a non-destructive chemical analysis technique that provides information about the molecular composition of a sample. When the light is directed towards a sample, most of it is scattered with the same energy and wavelength. However, in 1 over 10^7 photons, an energy exchange occurs between the incident photon and the molecules of the sample, which causes the shift of the photon's wavelength (Raman effect). Many vibrational spectroscopy techniques such as Raman spectroscopy [9–21], surface-enhanced Raman scattering (SERS) [22–24], surface enhanced resonance Raman scattering (SERRS) [25], coherent anti-Stokes Raman spectroscopy (CARS) [26–32], or stimulated Raman spectroscopy (SRS) [33–37] have been used to study the differences between brain cancer and healthy cells, not only in animals tissues, yet also in patients. For instance, using infrared Raman spectroscopy, Krafft et al. were able to map native brain tissue and tumors [9]. In the study carried out by Milena Köhler and collaborators, Raman spectroscopy and mass spectrometry were exploited to demonstrate that gliomas have a higher water content and a lowest lipid content with respect to porcine and human brain healthy tissues [10]. Besides, different studies have shown how Raman spectroscopy can be used to distinguish among white matter, gray matter, GBM, and necrotic tissue in frozen samples [14–16]. In the study carried out by Pinto Aguiar et al. [17] a model to discriminate between the spectra of normal tissue and of tumors was developed, based on the scores of principal component analysis (PCA) and Euclidean distance. Moreover, Galli et al. [19] were able to recognize non-neoplastic biopsies and tumor biopsies of different brain malignancies such as GBM, astrocytoma, oligodendroglioma, metastasis, meningioma, and schwannoma. In this sense, recent studies exploit discrimination models to determine molecular differences between normal and brain cancer cells [11,12,20,21].

In the last decade, several studies showed the possibility to delimit the tumor margins in animal models and tissues with the help of nanoparticles. As an example, Aydin et al. [22] were able to distinguish between healthy and peripheral tumor using silver nanoparticles in patient-derived tissue owing to the intensity ratio

of the peaks at 724 and 655 cm^{-1}, as well as to the appearance or the increase of other peaks at 558, 957, 1002, 1091, 1268, 1320, and 1366 cm^{-1} in the tumoral tissue. Furthermore, Kircher et al. showed that magnetic resonance-photoacoustic-Raman imaging nanoparticles can accurately help to delineate the margins of brain tumors in glioblastoma-bearing mice both preoperatively and intraoperatively [23]. The study performed by Huang et al. [25] found that the use of targeted nanoparticles (integrin-targeted gold core / silica shell nanoparticles) were able to (i) detect unexpected tumor areas distant from the main tumor, (ii) track migrating cells (clusters of 2–3 cells in diameter), and (iii) detect isolated distant tumor cell clusters of less than 5 cells. Additionally, another type of vibrational spectroscopy such as CARS has been used for imaging brain tumors not only in murine models [26–30] and pigs [31], yet but also in human tissue samples [29,31,32]. As a final example, SRS has been also used to identify brain tumors; in this case, the studies have been performed in mice [33], in human brain tissue [34–36], and even in a simulation of intraoperative pathologic consultation for 30 patients: indeed, Orringer et al. were able of discriminating the tumor mass from healthy tissue [37].

All these studies have demonstrated that molecular differences occur between healthy and cancer cells: for instance, the water content seems to be higher in cancer cells, and there are some peaks related to proteins (such as at 558, 957, 1002, 1091, 1268 and 1320 cm^{-1}) increased, as well as some related to DNA (723 cm^{-1}). In this study, we will analyze the differences between healthy astrocytes and four GBM patient-derived cell cultures by Raman spectroscopy, and, specifically, we will demonstrate that the region between 1000 and 1300 cm^{-1} could represent a single diagnostic window to classify healthy and glioma cells.

2. Material and methods

2.1. Patient-derived cultures

Four glioma biopsies (III-IV grade), derived from 4 different male patients, were collected from San Martino Hospital, Genova, Italy, in accordance to the procedure approved by the local ethical committee (*Registro CER Liguria* 341/2019). Despite there might be biological differences between male and female samples, we focused on male samples due to a relatively higher incidence in
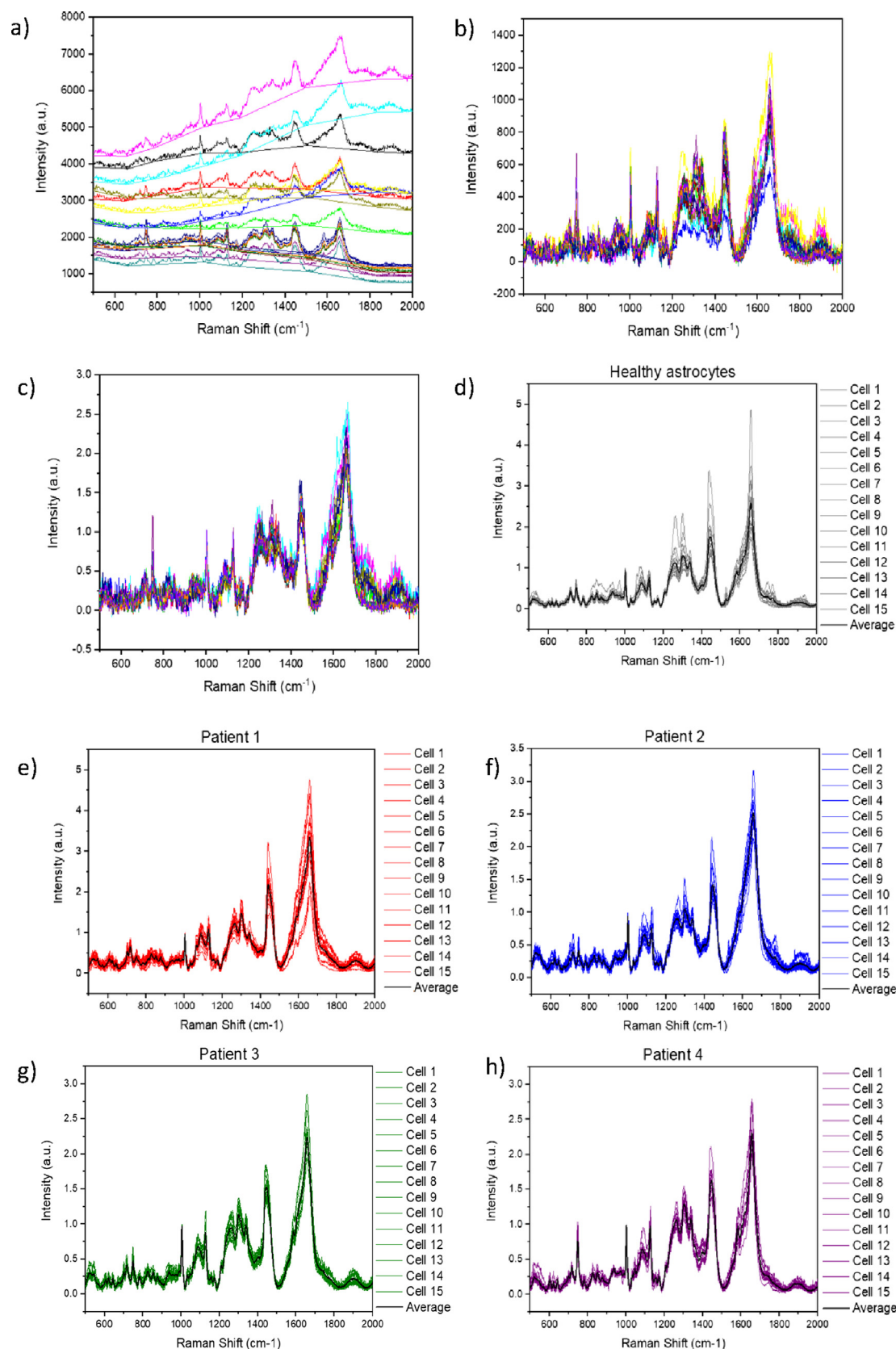
Fig. 2. Processing of the data before the analysis. (a) Original spectra plus the baseline of the 15 points of a single healthy astrocyte as an example; (b) spectra of a single cell after the baseline correction; (c) the same spectra after the normalization; (d) the average of each cell after the baseline correction and normalization; (e) the average of each cell from patient 1 after baseline correction and normalization; (f) the average of each cell from patient 2 after baseline correction and normalization; (g) the average of each cell from patient 3 after baseline correction and normalization; (h) the average of each cell from patient 4 after baseline correction and normalization. The overall average of all cells is depicted in black.

Fig. 3. Average spectra (with standard deviation) of astrocytes and of GBM patient-derived cells. The spectra have been obtained from the average of 15 cells for each type of cultures.
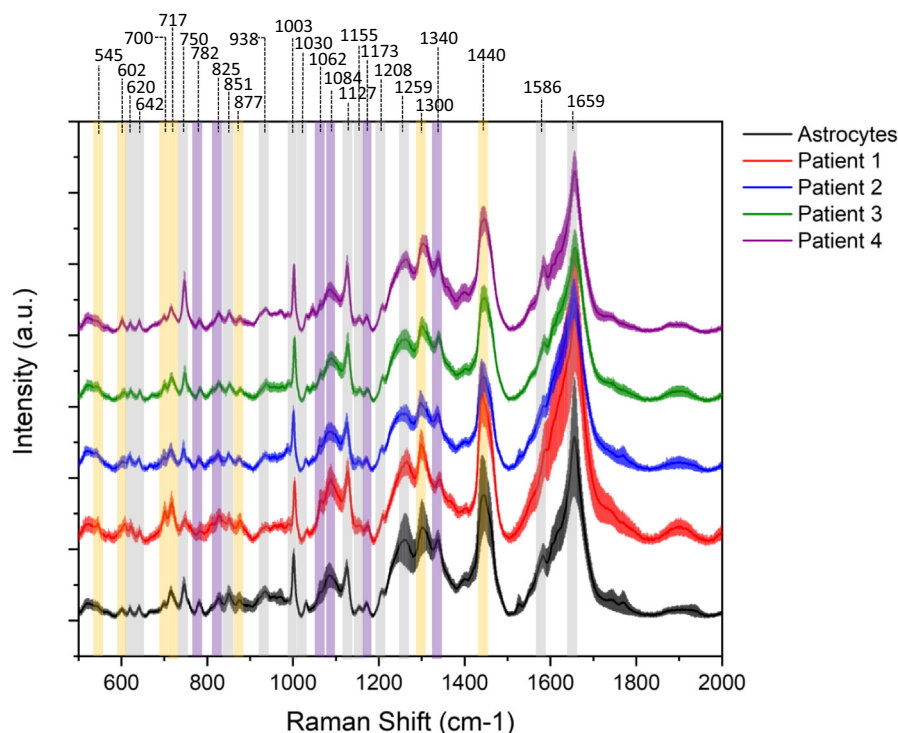
this population. The biopsies were washed twice with PBS with calcium and magnesium (Merck) and cut in small pieces with a scalpel. Thereafter, a passage in a 70 μm cell strainer (Corning) was performed, and the cell suspension was placed in culture with 10 ml of DMEM with 4.5 g/L glucose (Gibco), 10% fetal bovine serum (FBS, Merck), 1% L-glutamine (Gibco), and 1% penicillin/ streptomycin (Gibco). Obtained cultures have been progressively washed with daily rinsing in PBS to remove any residue, and finally split 1:3 for sub-culturing by using 0.05% trypsin.

Healthy human brain astrocytes (Alphabioregen) were instead cultured on Petri dishes previously treated with a specific coating for astrocytes (Alpabio Coat, Alphabioregen) with Astrocytes Growth Medium (Alphabioregen).

2.2. Raman measurements

Raman spectra were obtained using a Horiba LabRAM HR Evolution Raman microscope equipped with 532 nm laser and a laser power of 10%. In this work, different cell cultures have been used: healthy astrocytes at passage 3 and four different GBM patient-derived cultures at passages 3–4. Each type of cells was seeded on CaF$_2$ substrates, and for each group 15 cells were analyzed. The Raman spectra of each cell was obtained with the average of 15 point-spectra in each cell; the acquisition was done with a 60× immersion objective, with 3 accumulations of 30 s each.

2.3. Data analysis

Raman spectral data analysis was performed with OriginPro 2018. To achieve reproducible, qualitative, and quantitative data, the spectra were first processed through (i) baseline correction to remove spectral contributions due to fluorescence, and (ii) normalization with the band at 1003 cm^{-1} of phenylalanine [38,39].

2.3.1. Principal component analysis (PCA)

For chemometrics analysis, a Raman spectral dataset was prepared for principal component analysis (PCA): as mentioned before, in each group 15 cells were assessed. This analysis reduces the number of parameters needed to represent the variance in the spectral data set, performing a linear decomposition of signals in component vectors (principal components, PC) and scores [40]. Knowing the PC vectors, the importance of each PC in the formation of the spectrum of a particular sample can be established, and then this information (presence or absence of that particular feature in one group) can be exploited to classify the spectra into predetermined categories [17].

2.3.2. Linear discriminant analysis (LDA)

We used a predictive model composed by the discrimination function based on the linear combination of predictor variables that provide the best discrimination among cell types. To construct the discrimination model, the principal components scores (PC1 and PC2) were selected as independent variables. The linear discriminant analysis (LDA) model was created using 67% (10 spectra) of the dataset (training set), and validated against 33% (5 spectra) of the dataset (test set).

3. Results and discussion

3.1. Raman spectra of healthy cells vs. GBM patient-derived cells

The objective of the work was to discriminate between healthy astrocytes and GBM patient-derived cells. Fig. 1 shows a representative image of all the cell cultures used in this study. As mentioned in the material and methods section, 15 spectra *per* cell, on a total of 15 cells, have been acquired for each culture.

After the acquisition of all the spectra and before the analysis, the data were first processed. As reported in Fig. 2, a baseline correction was initially performed (Fig. 2a-b), and, subsequently, the

Table 1
Tentative assignment of the main Raman shifts according to the literature.

Raman Shift (cm^{-1})	Molecule	Ref.
545	Cholesterol	[17]
602–609	Cholesterol	[17]
620	C—C twist aromatic ring (Phe)	[22,41]
642	C—C twisting mode of tyrosine	[41]
700	Cholesterol	[9,17,41]
717	Choline group	[9,41]
750	Cytochrome *c*	[43]
781–782	DNA/RNA	[41]
825–827	O-P-O stretch DNA	[13,41]
851–855	C—C stretching of pro and CCH deformation ring breathing of tyr (protein); sterol ring stretch of cholesterol; glycogen	[13,17]
877	Choline and phospholipids	[11,13]
938	C—C stretching (amide III) – protein	[9,17,41]
1003	νs(C—C) phenylalanine ring breathing mode	[9,13,17,22, 41–43]
1030–1032	Phenylalanine (protein assignment) and collagen	[13,17,41]
1062	O-P-O stretch in DNA and RNA	[9,17,41,42]
1084–1086	Nucleic acids; C—C and C—O stretching modes in phospholipids	[17,41,42]
1127	Cytochrome *c*	[43]
1155	C—C (&C—N) stretching of proteins, Carotenoids	[41,43]
1173–1175	Cytosine, guanine	[41]
1208	Protein (Phe, Tyr)	[9,22,41]
1259	Amide III	[41]
1300	CH$_2$ and =CH bending of cholesterol; CH$_2$ deformation of saturated/unsaturated fatty acids; phospholipids (sphyngomyelin/ phosphatidylcholine/phosphatidylethanolamine)	[17,41,42]
1340	Nucleic acid mode	[13,41]
1440	Lipid d(CH$_2$)	[9,41]
1586	Cytochrome *c*	[43]
1659	Amide I (α-helix)	[9,11,13,17,41]
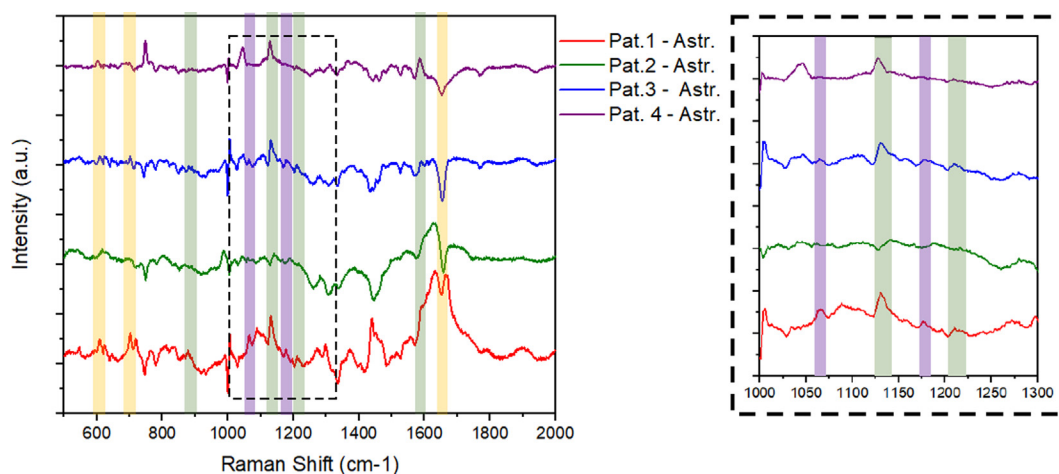
Fig. 4. Average Raman spectra of the 4 patient-derived cultures after the subtraction of the astrocyte spectrum. In the right part of the figure a zoom of the Raman shift from 1000 to 1300 cm^{-1} is reported.

intensity of individual Raman spectra was normalized to the band of phenylalanine (at 1003 cm^{-1}; Fig. 2c). Fig. 2d-h depict the spectra acquired, respectively, on healthy astrocytes, patient 1, patient 2, patient 3 and patient 4 after the data processing.

To better compare all spectra, we represented the average spectrum of each cell group in Fig. 3: in black the average with the deviation standar of healthy astrocytes, and in red, green, blue and purple the different patient-derived cells. The peaks related to lipids, proteins, and nucleic acids have been marked in yellow, grey, and purple, respectively. Regarding the lipids, for instance, the bands at 545, 602–609, 700, and 851–852 cm^{-1} can be associated to cholesterol [9,13,17,41]. Moreover, while the peaks at 717 and 877 cm^{-1} are related to choline group [9,11,13,41], the bands at 1300 and 1440 cm^{-1} are produced by C—H vibrations of acyl

chain CH$_2$ groups [13,17,41,42]. The band at 1084–1086 cm^{-1} can be attributed to the C—C and C—O stretching modes in phospholipids, but also to nucleic acids [17,41,42]. Besides, there are two band associated to the O-P-O stretch of DNA/RNA at 825–827 and 1062 cm^{-1} [9,13,17,41,42]. Concerning the nucleic acids, we can find three more bands at 781–782, 1173–1175, and 1340 cm^{-1} due to ring breathing modes in the DNA/RNA bases and the cytosine and guanine [13,41]. The rest of the peaks were associated to proteins or aminoacids. Indeed, the bands at 750, 1127, and 1586 cm^{-1} are assigned to cytochrome *c* [43]. Those ones at 620 and 640 cm^{-1} are due to the C—C twisting of aminoacids [22,41], while the peaks at 938 and 1259 cm^{-1} are associated to amide III [9,17,41]; the band at 1659 cm^{-1} is instead related to amide I [9,11,13,17,41]. To conclude, the peaks at 1003, 1030–
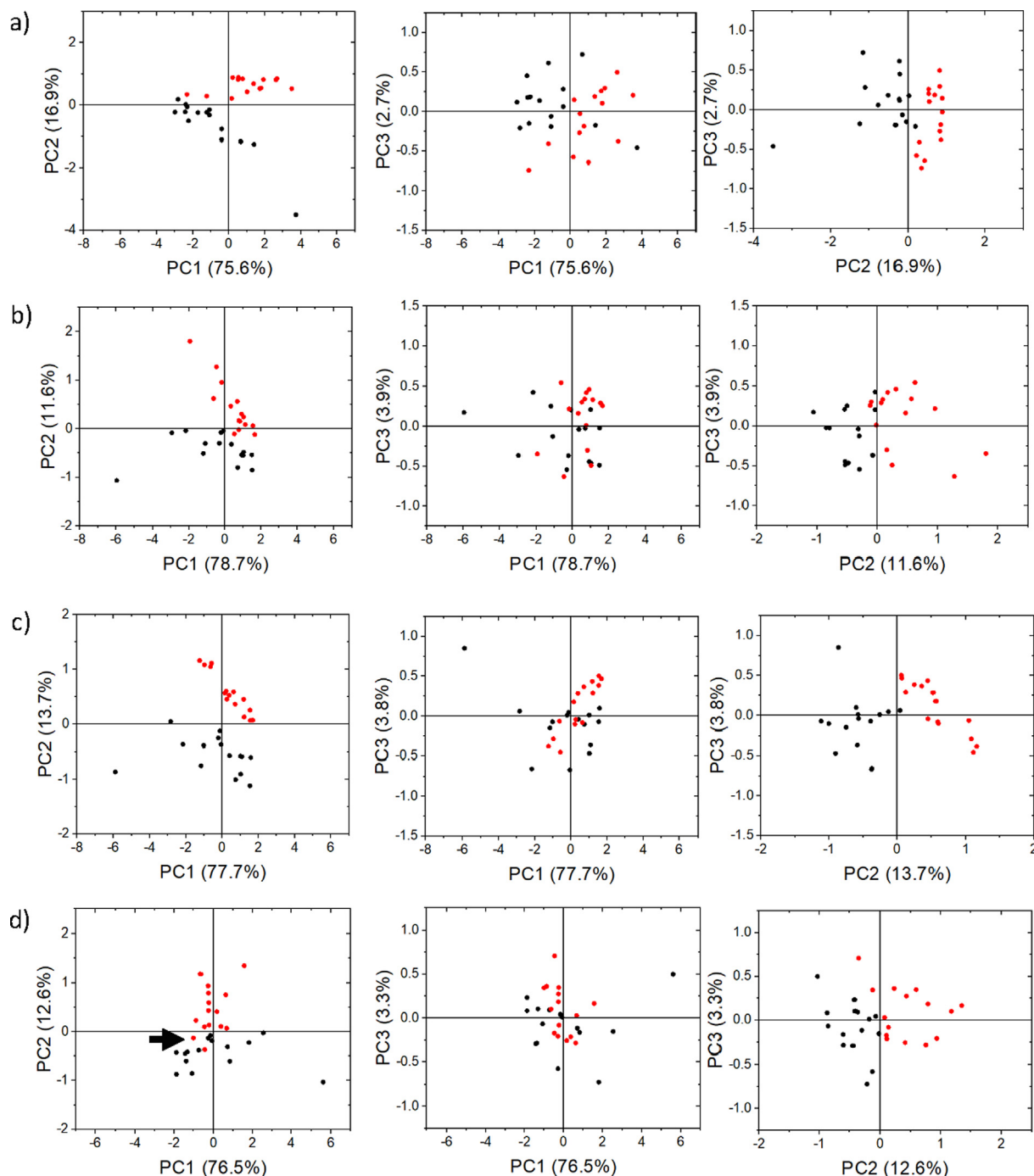
Fig. 5. Score plots of PCA models built with PC1/PC2 (left), PC1/PC3 (middle), and PC2/PC3 (right). (a) PCA model of astrocytes *vs.* patient 1, (b) PCA model of astrocytes *vs.* patient 2, (c) PCA model of astrocytes *vs.* patient 3, and (d) PCA model of astrocytes *vs.* patient 4. The contribution ratio of each component is shown in each axis. The black spots correspond to astrocytes, while the red spots to the patient-derived cells. (For interpretation of the references to colour in this figure legend, the reader is referred to the web version of this article).

1032, and 1208 cm⁻¹ are assigned mostly to phenylalanine [9,13,17,22,41–43], and the band at 1155 cm⁻¹ to C—C (and C—N) stretching of proteins and carotenoid [41,43]. Table 1 summarizes the tentative assignments of Raman peaks in all the cell types.

As we can deduce from Fig. 3, at first glance all spectra are very similar, which suggests that there might not be significant alterations in the overall molecular composition of lipids, nucleic acids, and proteins in healthy *vs.* GBM cells. Thus, to highlight the presence of small differences, we subtracted the astrocyte average to

the GBM patient-derived cells. As we can observe in Fig. 4, there are little but important differences: for instance, the small positive bands at 608 and 700 cm⁻¹ suggest highest amount of cholesterol content in cancer cells; this phenomenon has already been described in the literature [44,45]. Moreover, the sharp band at 1127 and at 1584 cm⁻¹ assigned to the cytochrome *c* could be associated with a higher number of mitochondrial contents, showing an increased metabolic activity in the cancer cells [43]. A weak positive band at 1062 and 1175 cm⁻¹ suggests a higher amount in nucleic acids content, and lastly, the negative peak at 1659 cm⁻¹
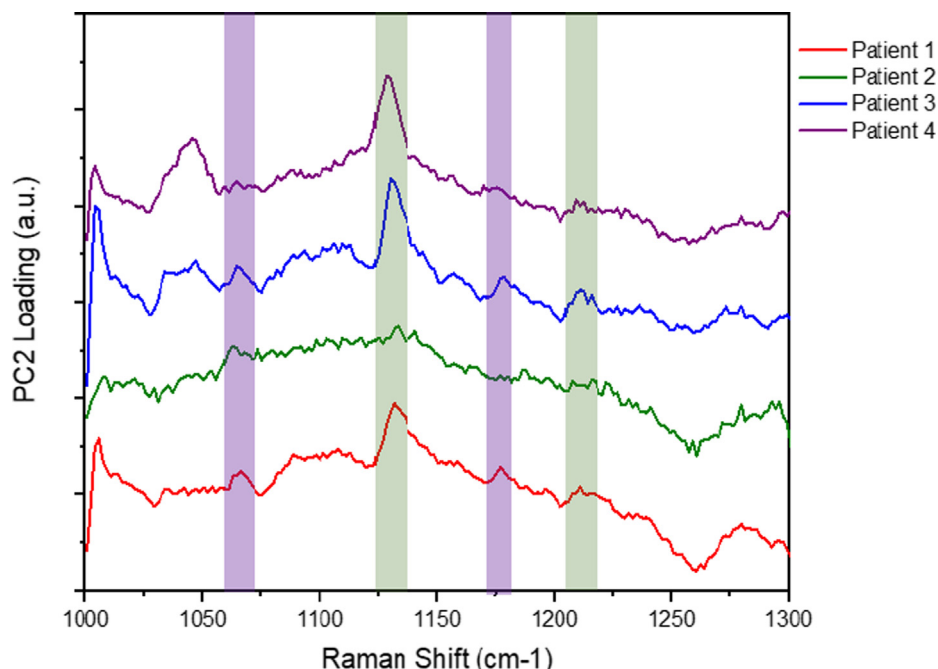
Fig. 6. Loading weight of PC2 in the following PCA models: astrocytes *vs.* patient 1, astrocytes *vs.* patient 2, astrocytes *vs.* patient 3, and astrocytes *vs.* patient 4.

Table 2
Discrimination of healthy astrocytes *vs.* GBM patient-derived cell lines *via* PCA-LDA.

Cell type	Raman diagnosis *via* PCA-LDA							
	1		2		3		4	
	Astr.	Pat.1	Astr.	Pat.2	Astr.	Pat.3	Astr.	Pat.4
Astrocytes	6	0	4	0	3	0	6	0
Patient1	1	3						
Patient2			0	6				
Patient3					0	7		
Patient4							2	2
Training Error	4.55 %		0 %		0 %		5 %	
Accuracy	90 %		100 %		100 %		80 %	

and the positive peaks at 877 and 1208 cm^{-1} could indicate a different protein and lipid composition; however, it is very difficult, at this stage, the indication of the involved proteins/lipids.

3.2. Discrimination based on PCA-LDA

As highlighted in the zoom of Fig. 4, differences regarding nucleic acids and proteins (cytochrome *c*) can be appreciated in the 1000–1300 cm^{-1} region. As it has been described in the literature, cancer cells usually have higher signal in the peaks related to nucleic acids and cytochrome *c* [43,46–48]. It is known that cancer cells proliferate in an uncontrolled manner, and have significantly increased intracellular DNA content, accompanied by substantial changes in phosphates, deoxyribose, or bases [46]. This phenomenon can explain the differences in the peaks related to DNA. Moreover, it has been demonstrated that a higher level of reduced cytochrome *c* might trigger a toxic runaway process and the progression of cancer development [48]; thus, this explains the higher intensity of the peak at 1127 cm^{-1}.

As there are important differences in this region (1000–1300 cm^{-1}), we wanted to show whether this would be enough to distinguish between healthy and cancer cells. At this aim, we firstly performed PCA classification models. It has been verified that the first 3 principal components carried around 92–95% of

all the spectral variation found in the data. Fig. 5 shows the score plots of PC1/PC2, PC1/PC3 and PC2/PC3, with the percentage of each PC in the axis, calculated for healthy astrocytes *vs.* (a) patient 1, (b) patient 2, (c) patient 3, and (d) patient 4 cell cultures. As it is shown in those score plots, the PC2 was the main contributor to the discrimination of cancer cells from astrocytes with minor overlap. Indeed, the representation of the loading weight of PC2 in the different PCA models (Fig. 6) resembles the different spectra shown in Fig. 3, showing that PC2 is responsible of the variation in those peaks. In fact, the bands in Fig. 5 have been mainly assigned to the O-P-O stretch in DNA and RNA, to the cytochrome *c*, to the cytosine and guanine content, and to proteins (phenylamine, tyrosine): 1063, 1129, 1175, and 1208 cm^{-1}, respectively. As previous studies have reported, the changes in proteins and nucleic acids in cancer cells can be detected by Raman spectroscopy, not only for brain cancers, yet also for other type of cancers such as breast cancer [42,43].

Following the PCA, linear discrimination analysis was performed. Table 2 shows the prediction of astrocytes *vs.* different patient-derived cells. In the first case, astrocytes *vs.* patient 1, the model was able to discriminate all the healthy cells correctly, and provided just one false negative error, which results into a diagnostic accuracy of 90%. When comparing patient 2 and 3 *vs.* healthy astrocytes, all samples were correctly classified, having

an accuracy of 100%. In the last comparison, the model for the astrocytes and patient 4 showed an accuracy of 80%, probably due to overlapping of two GBM cell spectra (Fig. 5d, left arrow).

In general, the results obtained in this study showed that Raman spectroscopy can identify changes in the molecular composition of healthy astrocytes compared to GBM patient-derived cells and that, associated with principal component followed by a linear discriminant analysis, can become a powerful and reliable tool for diagnosis.

4. Conclusions

The treatment of brain cancers and in particular of GBM is prompted to fail, as it is demonstrated by the low overall survival of the patients. As the main cause of mortality is due to cancer recurrence, there is a huge need for developing a tool that could accurately discriminate cancer from healthy tissue. This study showed that Raman spectroscopy is an effective technique for detecting biochemical changes between healthy and GBM cells. Moreover, the spectral analysis demonstrates that the range between 1000 and 1300 cm^{-1}, that includes changes in DNA/RNA and proteins (cytochrome c), could be enough for discrimination of cancer cells with an average accuracy of 92.5%: these results have been shown in 4 different male patient-derived cultures, confirming a reproducible method. Despite an analysis also on female patient-derived samples will be worth of investigation, cancer cells differ from normal cells mainly because of changes in proliferation rate (and thus in terms of DNA/RNA quantity) and in mitochondrial content (higher intensity in cytochrome c peak): we thus expect similar results also in female samples. Concluding, we believe that this achievement will help to further understand which are the essential Raman peaks for discriminating cancer from healthy cells, and thus, to improve diagnostic techniques with the final aim to enhance the overall survival of the patients.

CRediT authorship contribution statement

Nerea Iturrioz-Rodríguez: Conceptualization; Data curation; Writing - original draft. Daniele De Pasquale: Investigation; Methodology; Writing - original draft. **Daniele De Pasquale:** Resources; Project administration; Writing - review & editing. **Pietro Fiaschi:** Resources; Project administration; Writing - review & editing. **Gianni Ciofani:** Conceptualization; Project administration; Funding acquisition; Writing - review & editing.

Declaration of Competing Interest

The authors declare that they have no known competing financial interests or personal relationships that could have appeared to influence the work reported in this paper.

Acknowledgements

References

[1] J.P. Thakkar, T.A. Dolecek, C. Horbinski, Q.T. Ostrom, D.D. Lightner, J.S. Barnholtz-Sloan, J.L. Villano, Epidemiologic and molecular prognostic review of glioblastoma, Cancer Epidemiol. Biomarkers Prev. 23 (10) (2014) 1985–1996, https://doi.org/10.1158/1055-9965.EPI-14-0275.

[2] N. Iturrioz-Rodríguez, R. Bertorelli, G. Ciofani, Lipid-based nanocarriers for the treatment of glioblastoma, Adv. NanoBiomed Res. 1 (2) (2021) 2000054, https://doi.org/10.1002/anbr.v1.210.1002/anbr.202000054.

[3] A. Carrano, J.J. Juarez, D. Incontri, A. Ibarra, H. Guerrero Cazares, Sex-specific differences in glioblastoma, Cells 10 (2021) 1–22, https://doi.org/10.3390/cells10071783.

[4] L.P. Ganipineni, F. Danhier, V. Préat, Drug delivery challenges and future of chemotherapeutic nanomedicine for glioblastoma treatment, J. Control. Release. 281 (2018) 42–57, https://doi.org/10.1016/j.jconrel.2018.05.008.

[5] G. Minniti, D. Amelio, M. Amichetti, M. Salvati, R. Muni, A. Bozzao, G. Lanzetta, S. Scarpino, A. Arcella, R.M. Enrici, Patterns of failure and comparison of different target volume delineations in patients with glioblastoma treated with conformal radiotherapy plus concomitant and adjuvant temozolomide, Radiother. Oncol. 97 (3) (2010) 377–381, https://doi.org/10.1016/j.radonc.2010.08.020.

[6] M.C. Dobelbower, O.L. Burnett, R.A. Nordal, L.B. Nabors, J.M. Markert, M.D. Hyatt, J.B. Fiveash, Patterns of failure for glioblastoma multiforme following concurrent radiation and temozolomide, J. Med. Imaging Radiat. Oncol. 55 (2011) 77–81, https://doi.org/10.1111/j.1754-9485.2010.02232.x.

[7] M.C. Chamberlain, Radiographic patterns of relapse in glioblastoma, J. Neurooncol. 101 (2) (2011) 319–323, https://doi.org/10.1007/s11060-010-0251-4.

[8] K. Petrecca, M.-C. Guiot, V. Panet-Raymond, L. Souhami, Failure pattern following complete resection plus radiotherapy and temozolomide is at the resection margin in patients with glioblastoma, J. Neurooncol. 111 (1) (2013) 19–23, https://doi.org/10.1007/s11060-012-0983-4.

[9] C. Krafft, S.B. Sobottka, G. Schackert, R. Salzer, Near infrared Raman spectroscopic mapping of native brain tissue and intracranial tumors, Analyst 130 (2005) 1070–1077, https://doi.org/10.1039/b419232j.

[10] M. Köhler, S. Machill, R. Salzer, C. Krafft, Characterization of lipid extracts from brain tissue and tumors using Raman spectroscopy and mass spectrometry, Anal. Bioanal. Chem. 393 (5) (2009) 1513–1520, https://doi.org/10.1007/s00216-008-2592-9.

[11] J. Depciuch, B. Tołpa, P. Witek, K. Szmuc, E. Kaznowska, M. Osuchowski, P. Król, J. Cebulski, Raman and FTIR spectroscopy in determining the chemical changes in healthy brain tissues and glioblastoma tumor tissues, Spectrochim. Acta - Part A Mol. Biomol. Spectrosc. 225 (2020) 117526, https://doi.org/10.1016/j.saa.2019.117526.

[12] C. Robert, J. Tsiampali, S.J. Fraser-Miller, S. Neumann, D. Maciaczyk, S.L. Young, J. Maciaczyk, K.C. Gordon, Molecular monitoring of glioblastoma's immunogenicity using a combination of Raman spectroscopy and chemometrics, Spectrochim. Acta - Part A Mol. Biomol. Spectrosc. 252 (2021) 119534, https://doi.org/10.1016/j.saa.2021.119534.

[13] M. Riva, T. Sciortino, R. Secoli, E. D'amico, S. Moccia, B. Fernandes, M.C. Nibali, L. Gay, M. Rossi, E. De Momi, L. Bello, Glioma biopsies classification using raman spectroscopy and machine learning models on fresh tissue samples, Cancers (Basel) 13 (2021) 1–14, https://doi.org/10.3390/cancers13051073.

[14] R.E. Kast, G.W. Auner, M.L. Rosenblum, T. Mikkelsen, S.M. Yurgelevic, A. Raghunathan, L.M. Poisson, S.N. Kalkanis, Raman molecular imaging of brain frozen tissue sections, J. Neurooncol. 120 (1) (2014) 55–62, https://doi.org/10.1007/s11060-014-1536-9.

[15] S.N. Kalkanis, R.E. Kast, M.L. Rosenblum, T. Mikkelsen, S.M. Yurgelevic, K.M. Nelson, A. Raghunathan, L.M. Poisson, G.W. Auner, Raman spectroscopy to distinguish grey matter, necrosis, and glioblastoma multiforme in frozen tissue sections, J. Neurooncol. 116 (3) (2014) 477–485, https://doi.org/10.1007/s11060-013-1326-9.

[16] R. Kast, G. Auner, S. Yurgelevic, B. Broadbent, A. Raghunathan, L.M. Poisson, T. Mikkelsen, M.L. Rosenblum, S.N. Kalkanis, Identification of regions of normal grey matter and white matter from pathologic glioblastoma and necrosis in frozen sections using Raman imaging, J. Neurooncol. 125 (2) (2015) 287–295, https://doi.org/10.1007/s11060-015-1929-4.

[17] R.P. Aguiar, L. Silveira, E.T. Falcão, M.T.T. Pacheco, R.A. Zângaro, C.A. Pasqualucci, Discriminating neoplastic and normal brain tissues in vitro through raman spectroscopy: a principal components analysis classification model, Photomed. Laser Surg. 31 (12) (2013) 595–604, https://doi.org/10.1089/pho.2012.3460.

[18] H.N. Banerjee, A. Banerji, A.N. Banerjee, E. Riddick, J. Petis, S. Evans, M. Patel, C. Parson, V. Smith, E. Gwebu, S. Voisin, Deciphering the finger prints of brain cancer glioblastoma multiforme from four different patients by using near infrared Raman spectroscopy, J. Cancer Sci. Ther. 7 (2015) 44–47, https://doi.org/10.4172/1948-5956.1000323.

[19] R. Galli, M. Meinhardt, E. Koch, G. Schackert, G. Steiner, M. Kirsch, O. Uckermann, Rapid label-free analysis of brain tumor biopsies by near infrared Raman and fluorescence spectroscopy—a study of 209 patients, Front. Oncol. 9 (2019) 1165, https://doi.org/10.3389/fonc.2019.01165.

[20] N.M. Ralbovsky, I.K. Lednev, Raman spectroscopy and chemometrics: a potential universal method for diagnosing cancer, Spectrochim. Acta – Part A Mol. Biomol. Spectrosc. 219 (2019) 463–487, https://doi.org/10.1016/j.saa.2019.04.067.

[21] R.P. Aguiar, E.T. Falcão, C.A. Pasqualucci, L. Silveira Jr, Use of Raman spectroscopy to evaluate the biochemical composition of normal and tumoral human brain tissues for diagnosis, Lasers Med. Sci. (2020), https://doi.org/10.1007/s10103-020-03173-1.

[22] Ö. Aydin, M. Altaş, M. Kahraman, Ö.F. Bayrak, M. Çulha, Differentiation of healthy brain tissue and tumors using surface-enhanced Raman scattering, Appl. Spectrosc. 63 (10) (2009) 1095–1100, https://doi.org/10.1366/000370209789553219.

[23] M.F. Kircher, A. de la Zerda, J.V. Jokerst, C.L. Zavaleta, P.J. Kempen, E. Mittra, K. Pitter, R. Huang, C. Campos, F. Habte, R. Sinclair, C.W. Brennan, I.K. Mellinghoff, E.C. Holland, S.S. Gambhir, A brain tumor molecular imaging strategy using a new triple-modality MRI-photoacoustic-Raman nanoparticle, Nat. Med. 18 (5) (2012) 829–834, https://doi.org/10.1038/nm.2721.

[24] H. Karabeber, R. Huang, P. Iacono, J.M. Samii, K. Pitter, E.C. Holland, M.F. Kircher, Guiding brain tumor resection using surface-enhanced Raman scattering nanoparticles and a hand-held Raman scanner, ACS Nano. 8 (10) (2014) 9755–9766, https://doi.org/10.1021/nn503948b.

[25] R. Huang, S. Harmsen, J.M. Samii, H. Karabeber, K.L. Pitter, E.C. Holland, M.F. Kircher, High precision imaging of microscopic spread of glioblastoma with a targeted ultrasensitive SERRS molecular imaging probe, Theranostics 6 (8) (2016) 1075–1084, https://doi.org/10.7150/thno.13842.

[26] C.L. Evans, X. Xu, S. Kesari, X.S. Xie, S.T.C. Wong, G.S. Young, Chemically-selective imaging of brain structures with CARS microscopy, Opt. Express. 15 (19) (2007) 12076, https://doi.org/10.1364/OE.15.01207610.1364/OE.15.012076.m00110.1364/OE.15.012076.m002.

[27] O. Uckermann, R. Galli, S. Tamosaityte, E. Leipnitz, K.D. Geiger, G. Schackert, E. Koch, G. Steiner, M. Kirsch, Label-free delineation of brain tumors by coherent anti-stokes Raman scattering microscopy in an orthotopic mouse model and human glioblastoma, PLoS One 9 (2014), https://doi.org/10.1371/journal.pone.0107115.

[28] C.H. Camp Jr, Y.J. Lee, J.M. Heddleston, C.M. Hartshorn, A.R.H. Walker, J.N. Rich, J.D. Lathia, M.T. Cicerone, High-speed coherent Raman fingerprint imaging of biological tissues, Nat. Photon. 8 (8) (2014) 627–634, https://doi.org/10.1038/nphoton.2014.145.

[29] R. Galli, O. Uckermann, A. Temme, E. Leipnitz, M. Meinhardt, E. Koch, G. Schackert, G. Steiner, M. Kirsch, Assessing the efficacy of coherent anti-Stokes Raman scattering microscopy for the detection of infiltrating glioblastoma in fresh brain samples, J. Biophoton. 10 (3) (2017) 404–414, https://doi.org/10.1002/jbio.201500323.

[30] V.-H. Le, S.W. Yoo, Y. Yoon, T. Wang, B. Kim, S. Lee, K.-H. Lee, K.H. Kim, E. Chung, Brain tumor delineation enhanced by moxifloxacin-based two-photon/CARS combined microscopy, Biomed, Opt. Express. 8 (4) (2017) 2148, https://doi.org/10.1364/BOE.8.00214810.1364/BOE.8.002148.v00210.1364/BOE.8.002148.v001.

[31] T. Meyer, N. Bergner, C. Bielecki, C. Krafft, D. Akimov, B.F.M. Romeike, R. Reichart, R. Kalff, B. Dietzek, Jürgen Popp, Nonlinear microscopy, infrared, and Raman microspectroscopy for brain tumor analysis, J. Biomed. Opctics 16 (2) (2011) 021113, https://doi.org/10.1117/1.3533268.

[32] B.F.M. Romeike, T. Meyer, R. Reichart, R. Kalff, I. Petersen, B. Dietzek, J. Popp, Coherent anti-Stokes Raman scattering and two photon excited fluorescence for neurosurgery, Clin. Neurol. Neurosurg. 131 (2015) 42–46, https://doi.org/10.1016/j.clineuro.2015.01.022.

[33] M. Ji, D.A. Orringer, C.W. Freudiger, S. Ramkissoon, X. Liu, D. Lau, A.J. Golby, I. Norton, M. Hayashi, N.Y.R. Agar, G.S. Young, C. Spino, S. Santagata, S. Camelo-piragua, K.L. Ligon, O. Sagher, X.S. Xie, Rapid, Label-Free Detection of Brain Tumors with Stimulated Raman Scattering Microscopy, Sci. Transl. Med. 5 (2013) 1–10, https://doi.org/10.1126/scitranslmed.3005954.

[34] B. Sun, X. Wang, Z. Ji, M. Wang, Y.-P. Liao, C.H. Chang, R. Li, H. Zhang, A.E. Nel, T. Xia, NADPH oxidase-dependent NLRP3 inflammasome activation and its important role in lung fibrosis by multiwalled carbon nanotubes, Small 11 (17) (2015) 2087–2097, https://doi.org/10.1002/smll.201402859.

[35] F.-K. Lu, D. Calligaris, O.I. Olubiyi, I. Norton, W. Yang, S. Santagata, X.S. Xie, A.J. Golby, N.Y.R. Agar, Label-free neurosurgical pathology with stimulated Raman imaging, Cancer Res. 76 (12) (2016) 3451–3462, https://doi.org/10.1158/0008-5472.CAN-16-0270.

[36] T.C. Hollon, S. Lewis, B. Pandian, Y.S. Niknafs, M.R. Garrard, H. Garton, C.O. Maher, K. McFadden, M. Snuderl, A.P. Lieberman, K. Muraszko, S. Camelo-Piragua, D.A. Orringer, Rapid intraoperative diagnosis of pediatric brain tumors using stimulated Raman histology, Cancer Res. 78 (2018) 278–289, https://doi.org/10.1158/0008-5472.CAN-17-1974.Rapid.

[37] D.A. Orringer, B. Pandian, Y.S. Niknafs, T.C. Hollon, J. Boyle, S. Lewis, M. Garrard, S.L. Hervey-Jumper, H.J.L. Garton, C.O. Maher, J.A. Heth, O. Sagher, D.A. Wilkinson, M. Snuderl, S. Venneti, S.H. Ramkissoon, K.A. Mcfadden, A. Fisher-Hubbard, A.P. Lieberman, T.D. Johnson, X.S. Xie, J.K. Trautman, C.W. Freudiger, S. Camelo-Piragua, Rapid intraoperative histology of unprocessed surgical specimens via fibre-laser-based stimulated Raman scattering microscopy, Nat. Biomed. Eng. 1 (2017) 0027, https://doi.org/10.1038/s41551-016-0027.

[38] A. Fatima, G. Cyril, V. Vincent, J. Stéphane, P. Olivier, Towards normalization selection of Raman data in the context of protein glycation: application of validity indices to PCA processed spectra, Analyst. 145 (8) (2020) 2945–2957.

[39] R. Gautam, S. Vanga, F. Ariese, S. Umapathy, Review of multidimensional data processing approaches for Raman and infrared spectroscopy, EPJ Tech. Instrum. 2 (1) (2015), https://doi.org/10.1140/epjti/s40485-015-0018-6.

[40] I.T. Jolliffe, Principal Components in Regression Analysis, Springer-Verlag, New York, 1986.

[41] Z. Movasaghi, S. Rehman, I.U. Rehman, Raman spectroscopy of biological tissues, Appl. Spectrosc. Rev. 42 (5) (2007) 493–541, https://doi.org/10.1080/05704920701551530.

[42] W.C. Zúñiga, V. Jones, S.M. Anderson, A. Echevarria, N.L. Miller, C. Stashko, D. Schmolze, P.D. Cha, R. Kothari, Y. Fong, M.C. Storrie-Lombardi, Raman spectroscopy for rapid evaluation of surgical margins during breast cancer lumpectomy, Sci. Rep. 9 (2019) 1–16, https://doi.org/10.1038/s41598-019-51112-0.

[43] M. Kopec, M. Błaszczyk, M. Radek, H. Abramczyk, Raman imaging and statistical methods for analysis various type of human brain tumors and breast cancers, Spectrochim. Acta Part A Mol. Biomol. Spectrosc. 262 (2021) 120091, https://doi.org/10.1016/j.saa.2021.120091.

[44] J. Li, D. Gu, S S.-Y. Lee, B. Song, S. Bandyopadhyay, S. Chen, S.F. Konieczny, T.L. Ratliff, X. Liu, J. Xie, J.-X. Cheng, Abrogating cholesterol esterification suppresses growth and metastasis of pancreatic cancer, Oncogene. 35 (50) (2016) 6378–6388, https://doi.org/10.1038/onc.2016.168.

[45] G.W. Auner, S.K. Koya, C. Huang, B. Broadbent, M. Trexler, Z. Auner, A. Elias, K.C. Mehne, M.A. Brusatori, Applications of Raman spectroscopy in cancer diagnosis, Cancer Metastasis Rev. 37 (4) (2018) 691–717, https://doi.org/10.1007/s10555-018-9770-9.

[46] Y. Chen, J. Dai, X. Zhou, Y. Liu, W. Zhang, G. Peng, Raman spectroscopy analysis of the biochemical characteristics of molecules associated with the malignant transformation of gastric mucosa, PLoS One 9 (2014), https://doi.org/10.1371/journal.pone.0093906.

[47] Y. Oshima, H. Shinzawa, T. Takenaka, C. Furihata, H. Sato, Discrimination analysis of human lung cancer cells associated with histological type and malignancy using Raman spectroscopy, J. Biomed. Opt. 15 (1) (2010) 017009, https://doi.org/10.1117/1.3316296.

[48] H. Abramczyk, B. Brozek-pluska, M. Kopec, J. Surmacki, M. Błaszczyk, M. Radek, Redox imbalance and biochemical changes in cancer by probing redox-sensitive mitochondrial cytochromes in label-free visible resonance raman imaging, Cancers (Basel) 13 (2021) 1–20, https://doi.org/10.3390/cancers13050960.